Article

Precise Size Control of the Growth of Fe3O4 Nanocubes Over a Wide Size Range Using a Rationally Designed One-Pot Synthesis

Javier Muro-Cruces, Alejandro G. Roca, Alberto López-Ortega, Elvira Fantechi, Daniel del-Pozo-Bueno, Sònia Estradé, Francesca Peiró, Borja Sepúlveda, Francesco Pineider, Claudio Sangregorio, and Josep Nogues

ACS Nano, **Just Accepted Manuscript** • DOI: 10.1021/acsnano.9b01281 • Publication Date (Web): 07 Jun 2019

Precise Size Control of the Growth of Fe_3O_4 Nanocubes Over a Wide Size Range Using a Rationally Designed One-Pot Synthesis

Javier Muro-Cruces[1,2,*], Alejandro G. Roca[1,*], Alberto López-Ortega[3], Elvira Fantechi[4], Daniel del-Pozo-Bueno[5], Sònia Estradé[5], Francesca Peiró[5], Borja Sepúlveda[1], Francesco Pineider[4], Claudio Sangregorio[6,7], Josep Nogues[1,8]

[1]Catalan Institute of Nanoscience and Nanotechnology (ICN2), CSIC and BIST, Campus UAB, Bellaterra, 08193 Barcelona, Spain.

[2]Universitat Autònoma de Barcelona, 08193 Bellaterra, Spain

[3]Instituto de Nanociencia, Nanotecnología y Materiales Moleculares and Depto. de Física Aplicada, Universidad de Castilla-La Mancha, Campus de la Fábrica de Armas, 45071 Toledo, Spain

[4]Dipartimento di Chimica e Chimica Industriale and INSTM, University of Pisa, Via G. Moruzzi 13, 56124 Pisa, Italy

[5]LENS-MIND-IN2UB, Dept. Enginyeries Electrònica i Biomèdica, Universitat de Barcelona, Martí i Franquès 1, E-08028 Barcelona, Spain

[6]Dipartimento di Chimica and INSTM, Università degli studi di Firenze, Via della Lastruccia 3, Sesto Fiorentino (FI), I-50019, Italy

[7]ICCOM-CNR, Via Madonna del Piano, 10, Sesto Fiorentino (FI), I-50019, Italy

[8]ICREA, Pg. Lluís Companys 23, 08010 Barcelona, Spain

Corresponding authors mails: javimuroc@msn.com and alejandrogroca@gmail.com

ABSTRACT: The physicochemical properties of spinel oxide magnetic nanoparticles depend critically on both their size and shape. In particular, spinel oxide nanocrystals with cubic morphology have shown superior properties in comparison to their spherical counterparts in a variety of fields, like for example biomedicine. Therefore, having an accurate control over the nanoparticle shape and size, while preserving the crystallinity, becomes crucial for many applications. However, despite the increasing interest in spinel oxide nanocubes there are relatively few studies on this morphology due to the difficulty to synthesize perfectly defined cubic nanostructures, especially below 20 nm. Here we present a rationally designed, synthesis pathway based on the thermal decomposition of iron (III) acetylacetonate to obtain high quality nanocubes over a wide range of sizes. This pathway enables the synthesis of monodisperse Fe_3O_4 nanocubes with edge length in the 9-80 nm range, with excellent cubic morphology and high crystallinity by only minor adjustments in the synthesis parameters. The accurate size control evidences that even 1-2 nm size variations can be critical in determining the functional properties *e.g.*, for improved nuclear magnetic resonance T_2 contrast or enhanced magnetic hyperthermia. The rationale behind the changes introduced in the synthesis procedure (*e.g.*, the use of three solvents or adding Na-oleate) is carefully discussed. The versatility of this synthesis route is demonstrated by expanding its capability to grow other spinel oxides as Co-ferrites, Mn-ferrites and Mn_3O_4 of different sizes. The simplicity and adaptability of this synthesis scheme may ease the development of complex oxide nanocubes for a wide variety of applications.

KEYWORDS: magnetic nanoparticles, nanoparticles synthesis, magnetic hyperthermia, magnetic resonance imaging, iron oxides, nanocubes, anisometric nanoparticles

Nanoparticles have attracted an enormous interest during the last decades due to their appealing properties which have led to countless applications in very widespread fields. Interestingly, the physicochemical properties of nanoparticles (*e.g.*, magnetic, catalytic, optical, dielectric or thermal) can be efficiently tuned by designing not only their size but also their shape.[1,2] In particular, magnetic nanoparticles have been the subject of intense investigation in both industry and research due to their appealing and versatile properties[3] and the numerous applications (*e.g.*, information storage,[10] catalysis,[4] environmental remediation,[5] sensor technologies[6] or biomedicine[7] among many others). Specifically, for clinical applications iron oxides, magnetite (Fe_3O_4) and maghemite (γ-Fe_2O_3), are becoming the preferred material due to their excellent biocompatibility,[8,9] being the only magnetic materials approved by the US Food and Drug Administration (FDA) for the use in humans.[10]

Most of the research performed in maghemite/magnetite nanoparticles has been carried out on isotropic spherical particles.[8,9] However, recent studies have shown that anisotropic iron oxide nanoparticles have advantages in many applications over spherical ones, like longer blood circulation times,[11] higher surface to volume ratio allowing a better biomolecule grafting for targeting[12] and enhanced magnetic hyperthermia[13] or magnetic resonance imaging.[14] This improved performance is boosting the interest in non-spherical Fe_3O_4 nanoparticles. Nevertheless, the synthesis of Fe_3O_4 anisotropic nanoparticles is far more challenging than the spherical ones, since magnetite has a cubic crystal structure and, consequently, isotropic growth is more favoured.[15] In the particular case of nanocubes, it is important to emphasize that for an equal volume, cubes have a larger surface than spheres, which may be advantageous for many applications (*e.g.*, protein grafting or catalysis). Besides, the magnetic properties are also different, since the cubic morphology leads to an increase of both shape and surface anisotropies, which affects the superparamagnetic blocking temperature[16] or the Verwey transition.[13,17]

The synthesis of magnetite nanocubes has been attempted using different approaches. For example, magnetotactic bacteria can naturally synthesize magnetite nanocubes from 30 to 180 nm.[18] However, the process is slow (considering it requires working with cell cultures), not scalable and the size control is quite poor. Alternatively, chemical approaches include both aqueous[19] and organic-based syntheses.[12,20,21] The synthesis of nanocubes in aqueous media also requires a long time since the growth mechanism (and, hence, the control of the size and shape) is not trivial; subtle changes in the experimental conditions, which are difficult to control, can drastically affect the particle size and the size distribution.[19]

On the other hand, thermal decomposition of organic iron precursors represents a significant advance in controlling the size of iron oxide nanoparticles, with improved crystallinity and a narrow size distribution. Most of these syntheses use either iron (III) oleate or iron (III) acetylacetonate as iron precursor.[12,20,21]

In the first case, iron (III) oleate is decomposed in non-polar solvents (typically 1-octadecene, squalene or eicosane) in the presence of sodium oleate, and the size can be finely tuned from 9 to 23 nm,[21] reaching exceptionally larger sizes, up to 45 nm.[22–24] However, this synthesis involves the preparation of iron (III) oleate in a previous step, which unfortunately increases the required synthesis time and may lead to some variability between syntheses. Indeed, recent studies have reported that traces of chlorine ions remaining in iron oleate or the extractive process used in its synthesis can dramatically influence the final nanoparticle structure.[25] Moreover, it has been reported that the final product of the synthesis, especially for large particle sizes, is often a mixture of wüstite (FeO) and magnetite forming a FeO/Fe_3O_4 core/shell system.[22,26] Annealing can be used to convert the FeO/Fe_3O_4 particles to pure Fe_3O_4, however, this leads to defects in the structure which can negatively affect the physicochemical properties.[26]

The second approach is using iron (III) acetylacetonate as precursor and dibenzyl ether as solvent in the presence of oleic acid as surfactant, which has the advantage of being a one-pot synthesis. This reaction is considerably faster than the one based on iron (III) oleate and yields typically very large particles with sizes of more than 100 nm.[20] The size can be reduced down to about 20 nm by replacing oleic acid by other ligands, such as decanoic[12] or 4-biphenylcarboxylic acid.[20] However, a lack of reproducibility and size/shape heterogeneity arises when trying to further decrease the average size below 20 nm, where the particles become octahedral in shape or the size distribution becomes broad. Moreover, the use of benzyl ether as solvent in the synthesis presents some problems related with its decomposition to benzaldehyde and benzyl benzoate at high temperatures, often leading to unreproducible syntheses.[27,28] In fact, there is no reported synthetic method that leads to magnetite nanocubes that cover the whole size range. So far, when smaller or larger particles than the optimal range of a specific synthesis were required, it was necessary to change the synthesis method, otherwise the cubic shape was not retained, the particles became polydisperse or the crystallinity worsened. Additionally, reaching sizes for Fe_3O_4 nanocubes below 20 nm remains a challenge when using iron (III) acetylacetonate. This range is of special interest since the transition from blocked to superparamagnetic state (which, for example, affects the colloidal stability) is expected to be around this size for Fe_3O_4.[13]

Hence, the current somewhat limited control in the growth of magnetite nanocubes over a broad range of sizes with good particle size distribution and high crystallinity using a single and fast synthesis pathway, clearly highlights the need to develop versatile synthetic approaches to grow Fe_3O_4 nanocubes.

Here we propose a rationally designed, reproducible, one-pot synthesis of pure magnetite nanocubes from 9 to 80 nm in edge length with excellent particle size distribution (polydispersity index, PDI < 10%) and good crystallinity over the whole range of particle sizes. This synthetic approach relies on

the use of a combination of different solvents together with the addition of sodium oleate to (i) avoid the dibenzyl ether chemical decomposition, thereby making the synthesis more robust and reproducible, and (ii) regulate the chemical potential of the monomers favouring the cubic structure, keeping it even for small sizes, with a very narrow size distribution.

RESULTS AND DISCUSSION

Standard synthesis

The transmission electron microscopy (TEM) images of the nanocubes obtained from the standard synthesis (see METHODS) (Figure 1a,b) reveal a well-defined cubic structure with an edge length of 15.3±1.2 nm and a narrow particle size distribution, with a PDI of 8% (Figure 1c). Moreover, the scanning electron microscopy (SEM) images of the nanoparticles (Figure 1d) show very well ordered cubic superstructures, which confirms the good cubic shape and narrow particle size distribution of the nanocubes.[29]

The electron energy loss spectroscopy (EELS) analysis of the nanocubes at the Fe- and O-edges indicates that the samples are composed of Fe_3O_4 (Figure S1a,b). Importantly, the EELS mapping (Figure S1c) evidences that the oxidation state of the Fe atoms is homogenous over the whole particle, consequently ruling out any major presence of FeO at the core (due to incomplete reaction) or γ-Fe_2O_3 at the surface (because of surface oxidation).[23,30] Note that the EELS analysis also indicated the absence of sodium, excluding any impurities or inclusions within the nanostructures arising from the Na-oleate.

The x-ray diffraction (XRD) pattern (Figure S2) matches that of a cubic spinel lattice with a lattice parameter of a = 8.378(5) nm, consistent with Fe_3O_4 and γ-Fe_2O_3. In fact, the prominent peak at 18° indicates that the nanocubes are composed of Fe_3O_4 rather than γ-Fe_2O_3, in agreement with the EELS analysis. It is worth emphasizing that no other phases (*e.g.*, FeO) are present in the pattern. The crystallite size was evaluated using the Scherrer equation, giving a value of 14.6(4) nm. This value is quite close to the size obtained by TEM (15.3 nm), indicating that the particles are single-crystal.

The high crystallinity of the material was further confirmed by high resolution TEM (HRTEM) images, as shown in Figure 1e. The fast Fourier transform (FFT) of the image (Figure 1f) confirms the cubic spinel structure of the nanoparticles.

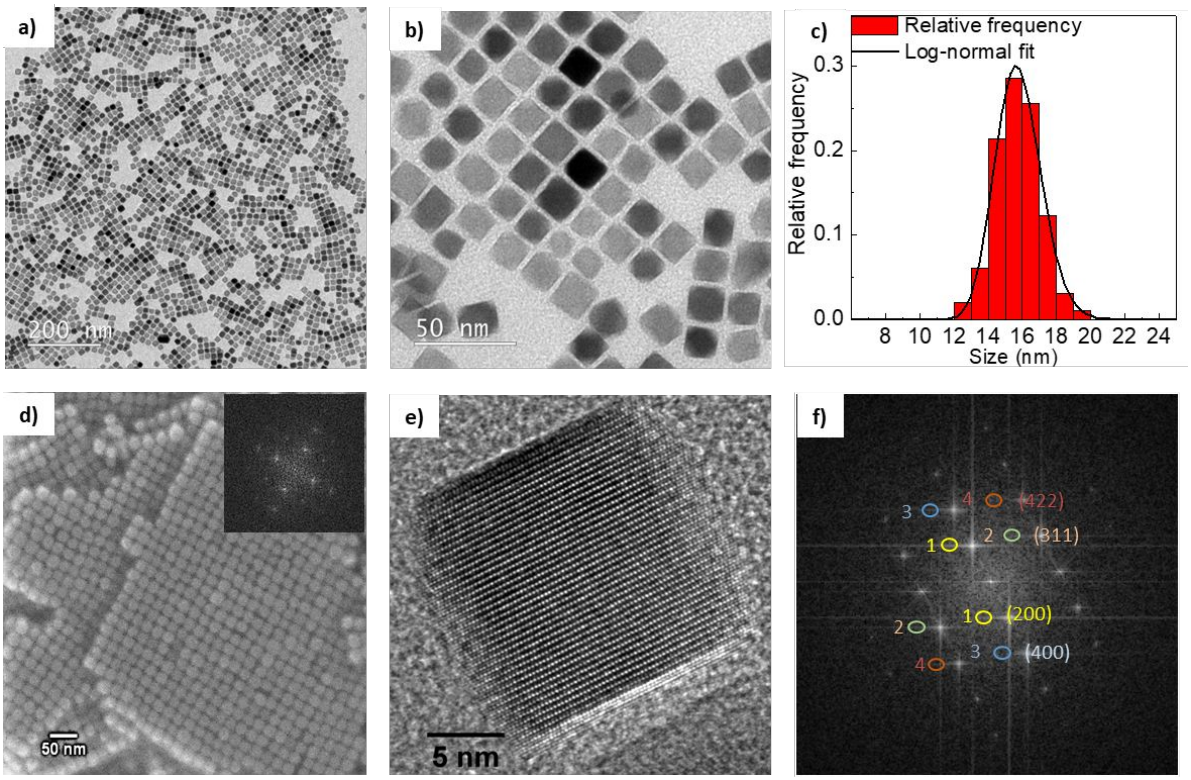

Figure 1. TEM images of the magnetite nanocubes obtained from the standard synthesis (a) at low magnification, (b) at high magnification. (c) Particle size distribution of the standard nanocubes and its fit to a log-normal function. (d) SEM image of the self-assembly of the nanocubes obtained from the standard synthesis. Shown in the inset is the corresponding FFT (which evidences a simple cubic symmetry). (e) HRTEM image of a single particle and (f) its corresponding FFT. The highlighted spots in (f) correspond to the expected cubic spinel (space group $Fd\bar{3}m$) (200) – 0.429 nm, (311) – 0.253 nm, (400) – 0.212 nm and (422) – 0.189 nm reflections seen along the [013] zone axis.

The magnetic measurements show that the saturation magnetization, M_S, of the nanocubes is 84 emu/g at room temperature rather close to the M_S of bulk magnetite (M_S ~ 90 emu/g), which further confirms the good crystallinity of the particles previously shown by XRD and HRTEM.

As expected from their size, the particles exhibit a superparamagnetic behaviour at room temperature (with negligible coercivity, $H_c \approx 0$ Oe and remanence, $M_r \approx 0$ emu/g; Figure 2a). As shown in the inset of Figure 2a, at 10 K the particles show a moderate coercivity (H_c = 200 Oe). Moreover, the temperature dependence of the magnetization, M(T), indicates that the blocking temperature, T_B (taken as the maximum in the zero field cooled magnetization curve; Figure 2b), is slightly above room temperature. In addition, M(T) exhibits a kink at low temperatures (Figure 2b). This is a prominent feature of the Verwey transition, which is typical for Fe_3O_4 but does not occur in γ-Fe_2O_3.[31] Thus, this confirms the EELS analysis that the nanocubes are pure Fe_3O_4.

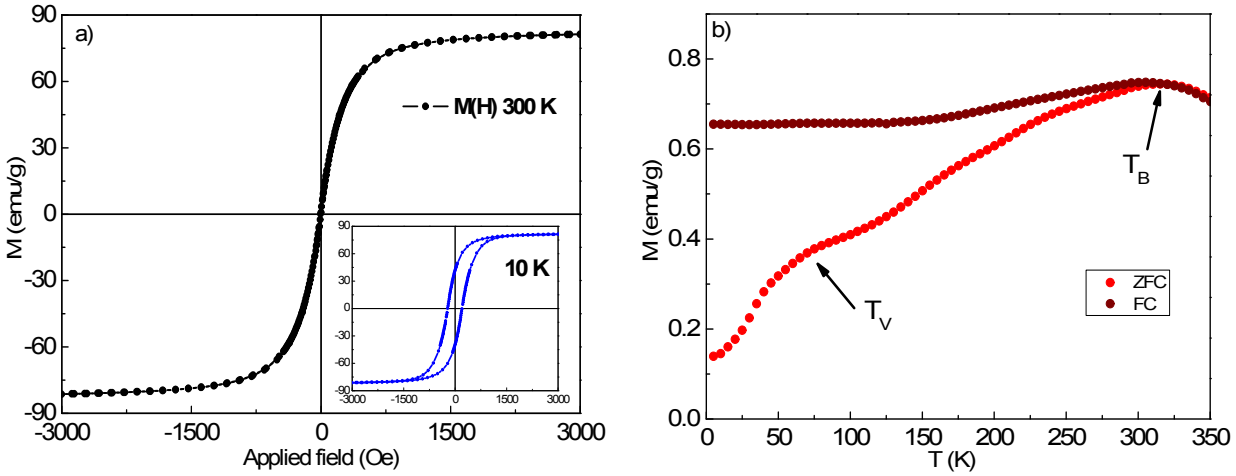

Figure 2. (a) Hysteresis loops at 300 K of the nanocubes obtained from the standard synthesis (15.3 nm). Shown in the inset is the loop at 10 K. (b) Temperature dependence of the field cooled (FC) and zero field cooled (ZFC) magnetization at H = 5 Oe. The blocking temperature, T_B, and the Verwey transition, T_V, are highlighted by arrows.

Size control

Several parameters were evaluated to control the particle size, such as solvent mixture polarity, boiling point, addition of a nucleation step, heating rate, temperature at which vacuum was performed, oleic/sodium oleate ratio, or solvent, among others (see Table S1). Notably, based on the standard synthesis described above, among all the tested parameters, the amount of iron acetylacetonate turned out to be the most convenient way to finely tune the size without losing the cubic shape. In fact, the particle size varies monotonically with the iron acetylacetonate amount (Figure 3f). For example, by decreasing the amount of iron acetylacetonate from 0.446 to 0.420 g the edge length decreases from 15.3 to 10.2 nm (Figure 3b), whereas when the iron acetylacetonate amount is increased to 0.61 g, the edge length increases to 24.5 nm (Figure 3c). However, if the iron acetylacetonate amount decreases exceedingly (below 0.420 g), although particle size can be further reduced to 9.1 nm, the cubic shape is partially lost, *i.e.*, the particles become more spherical and irregularly-shaped; (Figure 3a). Similarly, if too much iron acetylacetonate is used in the reaction, although the size does not change considerably (*e.g.*, 24.5 nm for 0.610 g of iron acetylacetonate), the particle shape tends to become more cuboctahedral in detriment of the cubic shape, as shown in Figure 3e).

As an alternative way to control the size, the temperature at which the vacuum stage was performed was changed between 100 ºC and room temperature achieving a final size of 11.8 nm and 23.7 nm,

respectively (Figures 3g,i). Nevertheless, similar to the control of the amount of iron acetylacetonate, this approach cannot be used to obtain particles larger than about 25 nm.

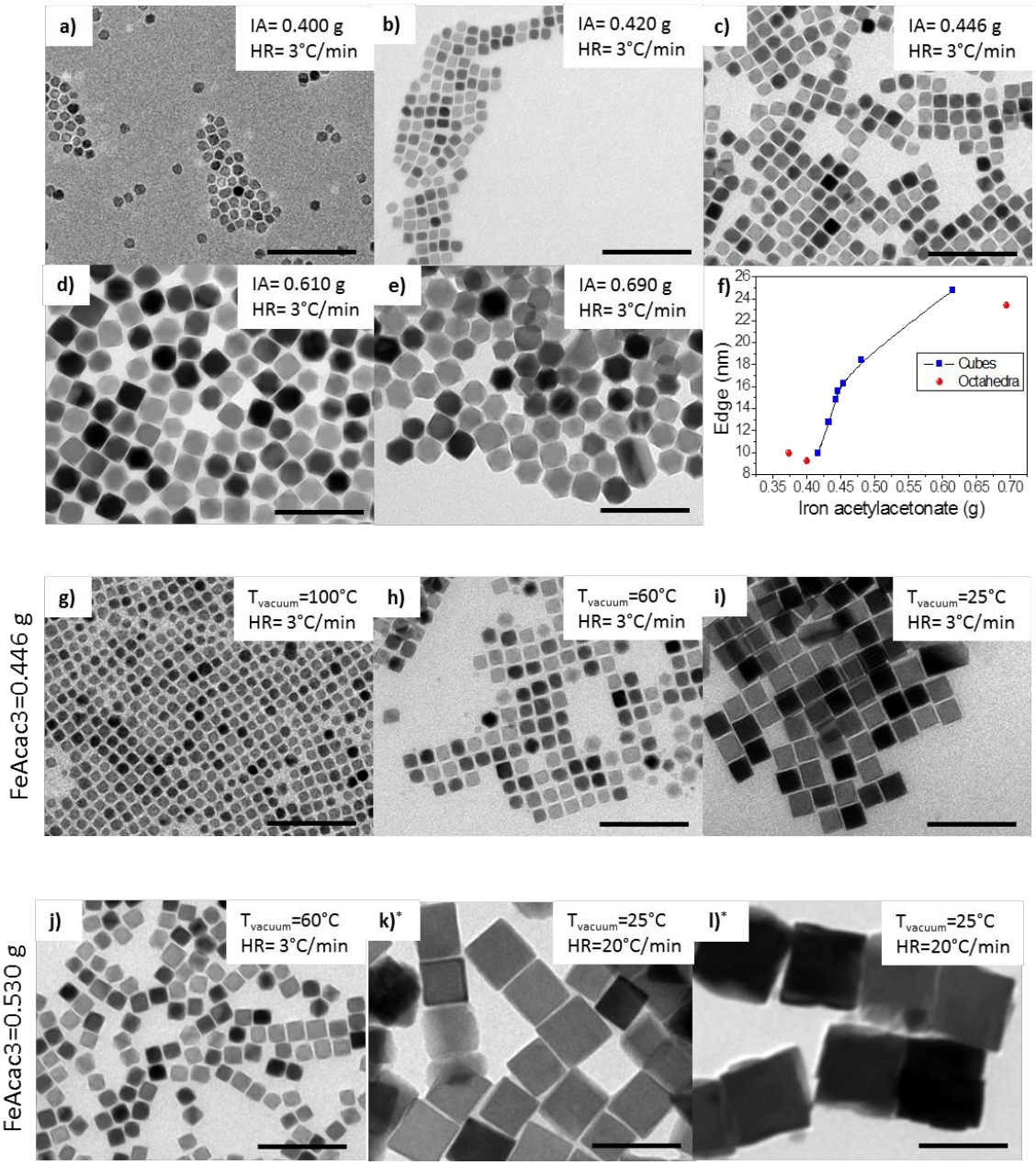

Figure 3. (a-e) TEM images of the effect of the iron acetylacetonate amount on the particle size and shape. (f) Dependence of the nanoparticle size on the amount of iron acetylacetonate. Note that the cubic particles are shown with blue squares, while other shapes are represented with red circles. (g-i) TEM images of the effect of temperature at which the vacuum stage is carried out for a fixed amount of iron acetylacetonate, FeAcac3 = 0.446 g. (j-l) TEM images of the effect of the heating rate carried out for a fixed amount of iron acetylacetonate, FeAcac3 = 0.533 g. "IA" and "HR" refer to iron acetylacetonate amount and heating rate, respectively. All the scale bars correspond to 100 nm.

*The syntheses corresponding to panels (k) and (l) were carried out in the same conditions but with different dilution factor; see Table S1.

Interestingly, this limitation can be overcome with only minor changes to the standard reaction and without changing any of the reactants. For example, a higher heating rate will produce a lower

number of nuclei that will have an increased chance for the iron to keep on growing. Thus, when 0.530 g of iron acetylacetonate were used with a heating rate of 3 °C/min, 17.4 nm cubes were obtained (Figure 3j). However, if the heating rate is increased to 15 °C/min, while keeping the rest of the conditions the same, particle size increases up to 25 nm (see Table S1). Importantly, increasing the total reagent concentration (*i.e.*, reducing the solvent volume) while applying a faster heating rate led to larger cubic particles. For example, if the heating rate is raised to 20 °C/min and the solvent volume is reduced to 17.3 mL (instead of 23 mL) the size increases to 52.6 nm (Figure 3k). Using an even smaller solvent volume (11.5 instead of 17.3 mL) while keeping the rest of the conditions the same, 80 nm cubes were obtained (Figure 3l).

Interestingly, the PDI of the nanoparticles was kept low across all the studied size range. Although the PDI reached a maximum of 14% for the largest sizes, it remained between 6-9% for the particles in the range from 9-53 nm (Figure 4, red symbols), thus they can be considered as monodisperse.

To assess the morphological quality of the particles, we used a simple "cubicity" parameter. Namely, since the ratio between the diagonal of a perfect square and its side is $\sqrt{2}$, by comparing the diagonal/side ratio with $\sqrt{2}$ we can have a quantitative idea on how close we are to an ideal-cube. Thus, while for a perfect cube the cubicity = diagonal/($\sqrt{2}$edge) × 100 should be 100%, for a sphere or a cuboctahedron the cubicity should decrease to 70% or 50%, respectively. Interestingly, the cubicity was beyond 90% throughout all the studied range (Figure 4), clearly indicating that cubic morphology is preserved.

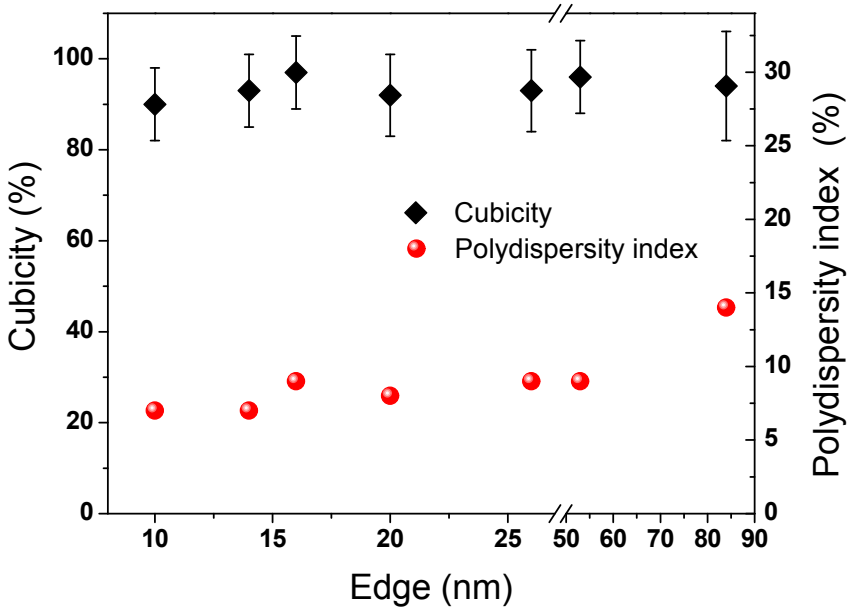

Figure 4. Cubicity (in black) and polydispersity index, PDI (in red) as a function of particle size. Note the break and the change of increment in the x-axis for large sizes.

Synthesis of other materials

To demonstrate the versatility of our synthetic approach we applied the same strategy to the synthesis of nanocubes of other metal oxide spinels such as cobalt and manganese ferrites (Figure 5). As an example of the easy size control without jeopardizing the morphology control, several sizes were obtained by controlling the temperature at which vacuum was performed.It is important to emphasize all the materials studied, the size polydispersity was kept at low values (7-16%) while preserving the cubic structure (as shown by the excellent cubicity), clearly evidencing the robustness of our synthesis pathway. Special mention deserves the synthesis of 6.7 nm manganese ferrite nanocubes with a clear cubic morphology. Note that the stoichiometry of both ferrites (1:2.2-Co:Fe for Co-ferrite and 1:2.8-Mn:Fe for Mn-ferrite, respectively; see SI) was close to the 1:2 ratio expected for ferrites, although no attempt was made to further optimize the composition.

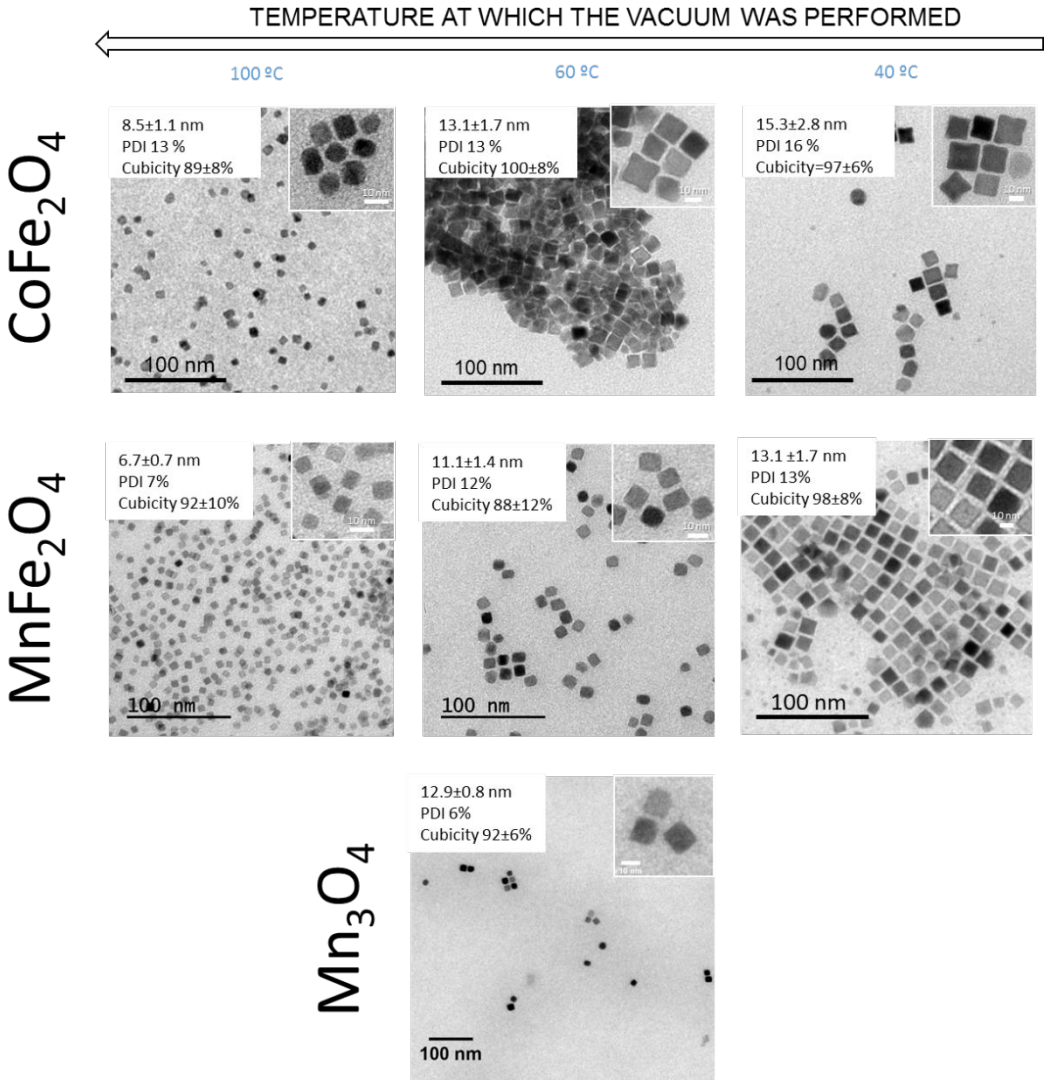

Figure 5. TEM images of cobalt ferrite nanocubes (upper row) of different sizes and manganese ferrite nanocubes (middle row) nanocubes of different sizes. The bottom row shows a TEM image of Mn_3O_4 nanoparticles.

Interestingly, a similar synthesis pathway was used to synthesize the tetragonal spinel Mn_3O_4. As can be seen in Figure 5, the synthesis results in excellent cubic particles also for non-cubic spinel structures. However, in this case the yield of the reaction is much lower than for Fe_3O_4, probably because all of the monomers are formed from a metal in a +2 oxidation state instead of +3, and hence there are not enough electron acceptors to favour the reaction.

Importance of the particle size on the colloidal stability

The achieved accurate control on the nanocubes size and the low PDI allow us to show the importance of the particle size on the colloidal stability of the magnetite suspensions. For many applications it is crucial to have colloidally stable nanoparticles for an optimum performance, especially for magnetic hyperthermia, drug delivery or magnetic resonance imaging, as uncontrolled irreversible aggregation will ruin their applicability. Stable single-particle colloidal dispersions are also necessary for an adequate water transfer of the nanoparticles for biomedical applications. To guarantee homogenous aqueous dispersions it is, therefore, key to ensure that the synthesis yields single particles, as the aggregated nanoparticles during the synthesis are hardly disaggregated in water. To verify whether the synthesis produces single-particles or aggregates, the hydrodynamic size was measured on freshly synthesized nanoparticles (*i.e.*, before transferring them to water). If particles are not aggregated, the ratio of the hydrodynamic and TEM particle sizes should be close to 1. Actually, a very abrupt change in the colloidal stability for particles larger than 16 nm is observed. Namely, while particles with sizes up to 16 nm showed a size ratio close to 1 (see inset in Figure 6), indicating that most of the cubes were in a single-particle state in dispersion, whereas for 17 nm particles and beyond aggregation is observed (Figure 6).

The degree of aggregation is probably related to the magnetic state[32,33] of the nanoparticles (see SI).

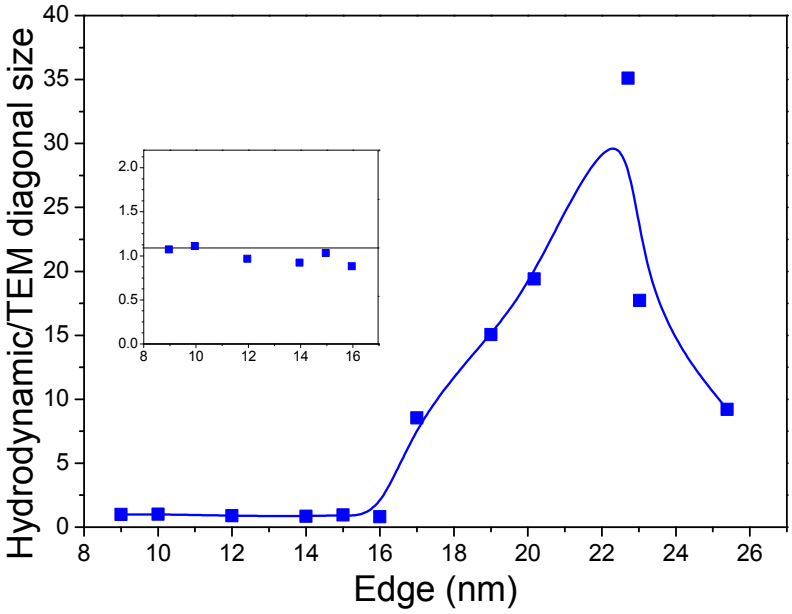

Figure 6. Hydrodynamic size/TEM diagonal as a function of the particle size. Shown in the inset is an enlargement for small sizes. Note that the diagonal rather than the edge length is used to account for the fact that the nanoparticles rotate during the hydrodynamic diameter measurements.

To have a more visual view of the effect of the colloidal stability, magnetite nanocubes within a range from 9 to 25 nm were dispersed and stored for 72 h. As can be seen in Figure S5, only particles with sizes below 17 nm remained stable.

This result highlights the relevance of the nanometric range size control to ensure the colloidal stability and, as it is shown below, to optimize the features for biomedical applications.

Importance of the nanocubes size for biomedical applications

To show the importance of the cube size for biomedical applications, the size dependence of the magnetic hyperthermia efficiency and magnetic resonance relaxivity of nanocubes for three different sizes (13.3, 15.3 and 19.3 nm) have been analysed. The nanocubes were first transferred into water by polymer-coating. It is important to mention that the morphology of the particles was examined after the transference process and no changes on either size or shape were observed (see Figure S6). After the transfer, the hydrodynamic size measurements showed that the particles remained in a single particle state, and the high Z-potential values (near -30 mV or beyond) indicated strong electrostatic interparticle repulsion (see Figure S7). The particle dispersions remained stable for at least several months, clearly evidencing the excellent colloidal stability of the nanoparticles.

To analyse the magnetic hyperthermia efficiency the nanocubes were exposed to an alternating field (H = 17 kA/m, frequency, f = 183 kHz). It is worth emphasizing that these conditions are rather mild, as the product H·f ($3.1 \cdot 10^9$ $A \cdot m^{-1} \cdot s^{-1}$) is clearly below the safety limit for clinical applications (*i.e.*, $5 \cdot 10^9$ $A \cdot m^{-1} \cdot s^{-1}$). Despite the moderate field, the heat generated after 5 min of magnetic actuation produced large temperature increases, ΔT, for the three particle sizes. It is worth highlighting that, under identical field and iron concentration (6.9 mg/mL), a size increase of just 2 nm (from 13.3 nm to 15.3 nm) induced an 85% enhancement of the ΔT (Figure 7). Moreover, the size increase up to 19 nm generated an additional 30% raise in the ΔT, which reached 65°C (Figure 7).[34] The specific absorption rate (SAR) values exhibited a similar tendency, showing a non-linear increase with the cube size. For example, an increase of only 2 nm in the particle size (from 13.3 to 15.3 nm) generates a 65 W/g gain in SAR, while an increase of 4 nm from 15.3 to 19.3 nm only leads to an increase of 17 W/g. Correspondingly, the intrinsic loss power (ILP) values obtained from the SAR were 2.08, 3.31 and 3.63 $nH \cdot m^2 \cdot kg^{-1}$ for the 13.3, 15.3 and 19.3 nm cubes, respectively. The non-linear SAR/ILP evolution is most likely linked to the transition between superparamagnetic and blocked states in the particles that was observed at a size of 16 nm.[12,35] Namely, the drastic increase in ΔT between the 13 and 15 nm samples is probably related to the fact that the 15 nm nanocubes are very close to becoming ferrimagnetic at room temperature. Hence, the application of an alternating field should induce considerable hysteresis losses in these particles. Interestingly, the ΔT and SAR values of the commercial Fe_3O_4 spherical particles (22±2 nm in diameter; Ocean Nanotech®; see SI), with a volume (5553 nm^3) slightly larger than the 15 nm cubes (3582 nm^3), measured in the same conditions, are considerably worse than those of the nanocubes (Figure 7). In fact, the ILP of the spherical nanoparticles, 1.1 $nH \cdot m^2 \cdot kg^{-1}$, is only one third of the one for the standard 15 nm nanocubes. Additionally, the ILP values of the nanocubes are also higher than the reported ones for commercially available Fe-based ferrofluids[36] and are comparable with other cubic iron oxide nanoparticles, which is an appealing result in view of the very mild conditions used in our study.[12,37,38] The results highlight the importance of the cubic morphology, good crystallinity, nanometric control of the size and lack of agglomeration to optimize the response for magnetic hyperthermia applications.[39,40]

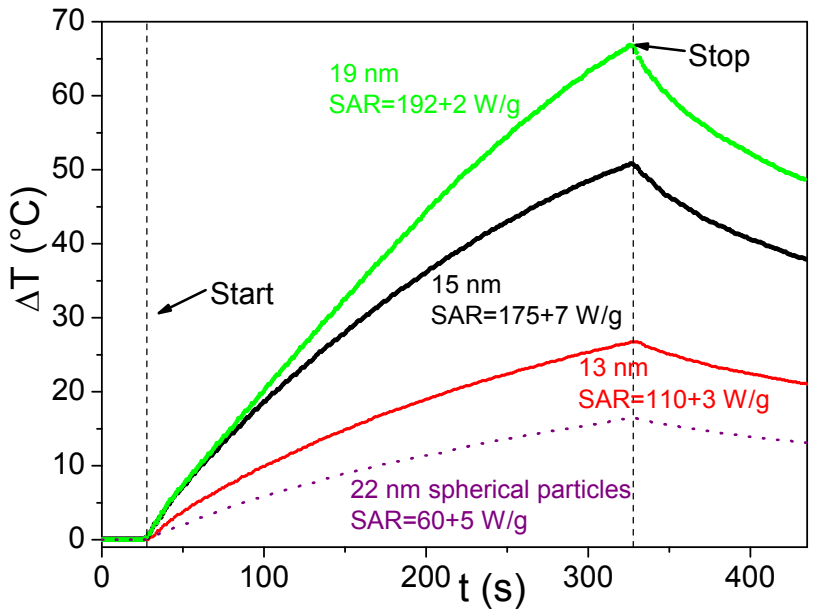

Figure 7. Temperature increase as a function of time for the different nanocubes and the commercial spherical particles exposed to an alternating magnetic field (17 kA/m – 183 kHz). "Start" and "Stop" indicate the beginning and the end of the application of the magnetic field.

.

On the other hand, the size effect on the nuclear magnetic resonance (NMR) response of the nanocubes was assessed by measuring the r_2 relaxivity for 13.3, 15.3 and 19.3 nm nanocubes. As can be seen in Figure 8, the increase in size from 13.3 to 15.3 nm enables a 40% enhancement in the r_2 value (from 332 to 455 $s^{-1}mM^{-1}$). However, a further increase to 19.3 nm has a minimal effect on r_2 (460 $s^{-1}mM^{-1}$). This is in agreement with earlier studies which reported a raise of r_2 with size for superparamagnetic nanoparticles and a saturation of r_2 as the particles become ferrimagnetic and evidences the importance of the size control also for NMR imaging.[41] These values were compared to those of commercial spherical particles of 22 nm in diameter (Ocean Nanotech®; see SI) which, despite having a similar volume to the 15 nm edge nanocubes, they showed a 1.6 times smaller r_2 value (293 $s^{-1}mM^{-1}$; Figure S9). Notably, the values for the nanocubes are considerably higher than commercially available contrast agents such as Feridex® and Resovist ®, whose r_2 values are 105 and 176 $s^{-1}mM^{-1}$, respectively.

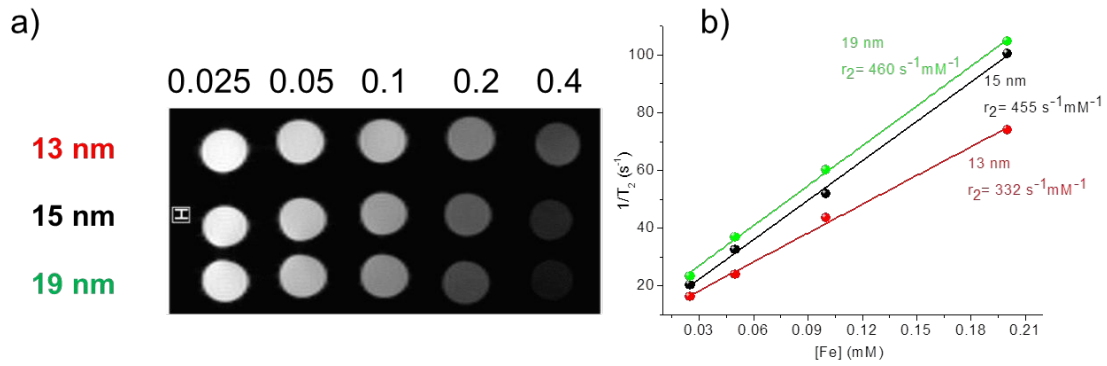

Figure 8. (a) T_2-weighted magnetic resonance images of agarose phantoms for nanoparticles of different sizes and different concentrations (the numbers above the image indicate the [Fe] concentration in mM). (b) Dependence of the NMR R_2 ($1/T_2$) values on the [Fe] concentration for the three samples.

Discussion of the synthesis protocol

Given the relevance of the size to maximize the performance in biomedical applications, it is worth discussing the rationale behind the achieved control in the nanocubes synthesis.

For equal volume, the surface-to-volume ratio of cubes is about 25% larger than for spheres. This implies a larger surface energy for cubes at all sizes. However, as the size of the nanocubes becomes smaller (particularly below 25 nm) the surface-to-volume ratio dramatically increases (see Figure S10). Consequently, cubic shapes become increasingly less energetically favourable than spherical ones as size decreases. Therefore, to synthesize nanocubes it is crucial to provide a chemically stable environment whose properties remain unchanged during the growth stage, since any perturbation can destabilize the growth of the particles leading to deviations in either the size or the shape towards other more thermodynamically favourable structures. Taking into account these aspects, we have carefully designed a chemical synthesis for magnetite nanocubes by rationally choosing the iron precursor, surfactants, solvents, heating rate and other steps of the reaction.

Thermal decomposition of metal organic precursors in the presence of fatty acids (commonly, oleic acid), which can act as both surfactant and reductor, represents a good synthetic strategy since it produces highly crystalline monodisperse particles with narrower size distribution than other methods like coprecipitation, microemulsions, laser or spray pyrolysis.[32] In the case of iron oxide nanoparticles, the most popular iron precursors are iron oleate, iron pentacarbonyl and iron acetylacetonate. Since iron oleate is not commercially available, it must be synthesized prior to the synthesis of the nanoparticles, which adds a tedious step to the synthesis process. Moreover, the exact details of the synthesis and purifying steps deeply affect the quality of the resulting nanoparticles, introducing a high degree of variability. Moreover, the synthesis often yields a mixture of several iron oxide phases rather than pure magnetite.[42] Iron pentacarbonyl generally leads to metallic iron particles which are further oxidized to magnetite or maghemite.[43] However, this compound is chemically

unstable and the crystallinity of the resulting nanoparticles is not very high.[44] On the other hand, iron acetylacetonate is a highly stable and a commercially available reagent, which makes it a more desirable candidate for the synthesis of high quality iron oxide nanoparticles.

Considering that thermal decomposition occurs at high temperature and iron acetylacetonate is a moderately polar molecule, a polar high-boiling solvent should be used. Thus, iron acetylacetonate is usually used with dibenzyl ether as solvent. However, dibenzyl ether has been reported to be unstable at high temperatures leading to benzaldehyde, especially in the presence of oxygen.[27,28] This instability results in dramatic changes of the solvent properties, like the polarity, boiling point or conductivity. For example, during the synthesis of iron oxide nanoparticles it has been observed that the boiling temperature of the mixture decays several degrees as the growth stage advances due to the emergence of more volatile molecules.[45] This lack of a stable environment for the growth of the particles hinders the formation of small monodisperse and well-defined cubic structures.

The key factors that determine the final structure of iron oxide particles synthesized by thermal decomposition have been studied in detail and some factors, like the ratio of oleic acid to iron, have been identified as critical.[46] However, Qiao *et al*. recently proposed that the final shape and size is determined mainly by the balance between the chemical potential of the monomers (μ_m, see below) and the chemical potential of the different crystal planes.[28] In the particular case of magnetite, the {111} planes are the most densely packed and have the lowest chemical potential.[47] On the other hand, the {100} planes are the least densely packed and have the highest reactivity, while the {110} planes have an intermediate packing and chemical potential. Therefore, the chemical potential of these planes can be ranked as: $\mu_{\{100\}} > \mu_{\{110\}} > \mu_{\{111\}}$.

Note that the chemical potential of the monomers is defined as $\mu_m = \mu_m^0 + RT\ln[C_m \cdot \gamma_m]$, where μ_m^0 is the chemical potential of the monomers in a reference state and is a constant; R is the ideal gas constant; T is for temperature; C_m is the concentration of monomers and γ_m *i*s the activity coefficient of the monomers in solution.

As the temperature of the mixture increases, the iron acetylacetonate exchanges iron cations with the oleate anions to form monomers.[48] These monomers accumulate and once oversaturation is reached, nuclei are generated.[49] At this point, the chemical potential of monomers is higher than those of the crystal planes ($\mu_m > \mu_{\{100\}} > \mu_{\{110\}} > \mu_{\{111\}}$) and they can change from the solvated state (high chemical potential) to any of the planes of lower chemical potential.[50] This stage is called diffusional growth. Although in nuclei all of these facets are exposed and thermodynamically the growth in any plane is permitted, the rate at which monomers are deposited is different for every facet and it depends on the kinetic constants, which are inversely proportional to the energy barrier of the process. Since the {111} planes are the most densely packed and thus they have a high steric hindrance, the arrival of new monomers will be inhibited. Therefore the energy barrier that monomers have to overcome to

deposit on this plane is higher than on the other planes, consequently the {111} facets will grow the slowest.

The initial simultaneous growth in the three directions (ruled only by the differences in deposition rates) leads to the formation of octahedrons (see Figure 9). As the reaction advances, the chemical potential of the monomers falls (*i.e.*, because of the C_m decay) to a point where the {100} planes cannot grow anymore ($\mu_{\{100\}} > \mu_m > \mu_{\{110\}} > \mu_{\{111\}}$). However, the {110} and {111} facets keep growing, which makes the octahedra turn into tetradecahedra (see Figure 9). Similarly, when the μ_m decays sufficiently, deposition on the {110} planes stops, while it continues on the {111} facets, leading to the transition from tetradecahedra into cubes (see Figure 9). If the amount of remaining monomers is sufficiently high to continue the deposition in {111} planes, the cubes vertices will continue to grow, resulting in star-like structures. However, because of the large hydrodynamic size of the iron oleate monomers it is very difficult for them to overcome the steric hindrance of the {111} planes making the growth of stars rather inefficient.

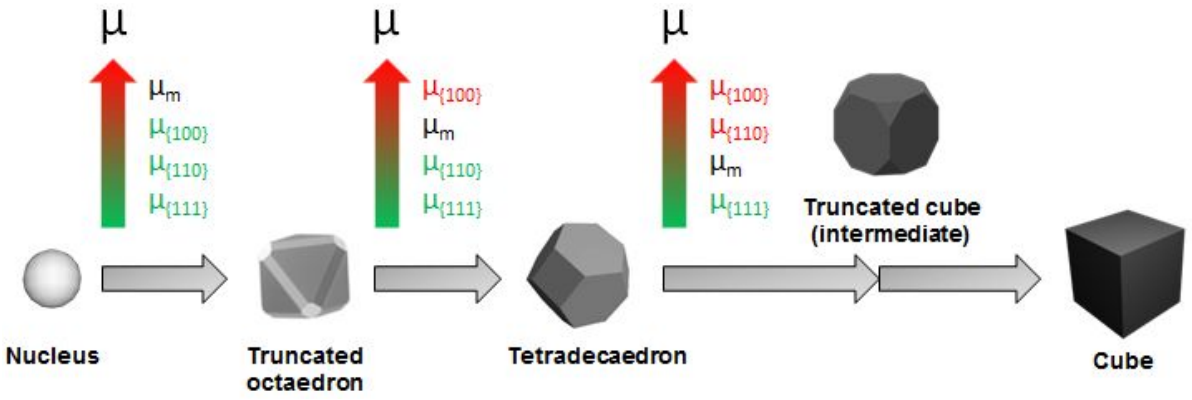

Figure 9. Schematic representation of the transition from a nucleus into a cube as μ_m decays. The green (red) colour for the μ of the crystal planes depends if their chemical potential is lower (higher) than μ_m.[28]

Since several parameters control the chemical potential of the monomers, μ_m, diverse approaches can be envisaged to engineer the morphology of the nanoparticles. However, μ_m^0 and R are constants and, thus they do not influence the shape of the particle. Additionally, taking into account that the growth stage is carried out at the boiling temperature of the solvent, if the solvent composition is stable, T can be considered as a constant that will be defined mainly by the properties of the solvent used for the synthesis. This implies that C_m and γ_m are the parameters than can be controlled to tune the chemical potential.

C_m is the balance between the rate at which monomers are generated and consumed during the synthesis. In our case, this can be controlled by the total amount of iron and surfactants and also by tuning the ratio between oleic acid and sodium oleate, as will be explained later. The other parameter, γ_m, depends on how strong is the interaction between the solvent and the monomers, and it can be adjusted by either changing the iron ligands or the solvent. Since non-polar solvents have stronger

molecular interactions with the long aliphatic chains of the monomers, they should decrease the activity coefficient of the monomers; consequently, they should ease the formation of cubic structures, while polar solvents should tend to favour octahedral-like structures. This effect becomes critical when using dibenzyl ether, since at high temperatures it usually decomposes into molecules like benzaldehyde, which are even more polar than the dibenzyl ether itself. As a consequence of this rise in polarity, interactions between the solvent and the aliphatic chains of the monomers become weaker, increasing γ_m, which in turn increases μ_m so much that the growth on all facets is permitted. This implies that although initially cubes can grow using dibenzyl ether, as it starts to decompose the morphology control is lost. In the extreme situation, eventually a secondary nucleation becomes possible, resulting in polydisperse particles.

Based on the above arguments, one could think that replacing dibenzyl ether for 1-octadecene, which is more stable and less polar, could be a good solution. However, replacing dibenzyl ether by 1-octadecene is not possible because iron acetylacetonate is poorly dissolved in such a non-polar solvent. Nevertheless, even if a total substitution of dibenzyl ether is not feasible, still a partial substitution is possible to minimize the effects of the dibenzyl ether instability. This is why in our approach we decided to use a mixture of 1-octadecene and the minimum amount of dibenzyl ether necessary to dissolve iron acetylacetonate. 1-octadecene has a higher boiling point than dibenzyl ether (315 vs 298 °C), consequently, the resulting mixture has an intermediate boiling point between both solvents. However, given the lability of the ether bond in dibenzyl ether, we considered it would be favourable to intentionally decrease the boiling temperature of the mixture to prevent the risk of dibenzyl ether decomposition. This is why 1-tetradecene was added to the mixture since it has a similar structure to that of 1-octadecene but with a much lower boiling point (252 °C). The volume of 1-tetradecene in the solvent mixture was adjusted so the overall boiling point of the mixture was around 290 °C. Importantly, the resulting solvent mixture showed a very stable boiling temperature over time, in contrast to pure dibenzyl ether as can be seen in Figure 10 and reported before.[27] Note that reaching the boiling temperature in the final step of the synthesis is highly desirable to induce a rapid oversaturation of monomers that triggers a burst homogeneous nucleation. It is important to stress that the nucleation does not occur only because a critical concentration of monomers is surpassed, but rather because of the sudden increase in the $\gamma_{Monomers}$ (and consequently their activity) when the solvent mixture starts to boil, which triggers the burst nucleation. This will make the nuclei appear mostly at the same time and to grow at the same rate, resulting in more monodisperse nanoparticles.[51] Another reason why it is advisable to reach such a high temperature is to promote the complete reduction of iron (III) to iron (II), a required step to form magnetite.[42]

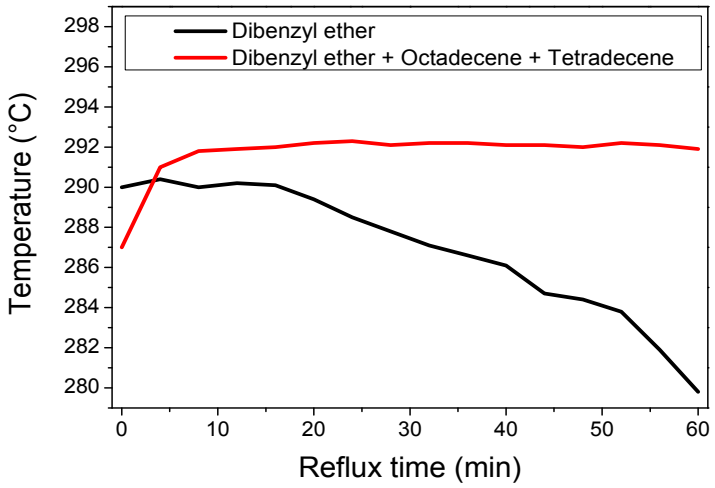

Figure 10. Evolution of the synthesis temperature with the reflux time for both dibenzyl ether alone and the solvent mixture described in the text.

As previously mentioned, controlling the chemical potential of the monomers during the growth stage is crucial to control the final shape of the particles. Based on this fact, we assumed that a more constant chemical potential of the monomers during the diffusion growth stage will produce better defined structures. For this reason we combined the use of oleic acid with its sodium salt, sodium oleate. Sodium oleate can also coordinate with iron but it must first dissociate from sodium. This dissociation is disfavoured in non-polar solvents, where it takes place only in a small proportion, slowing down the formation of monomers.

However, as the reaction proceeds and oleate anions are consumed, the dissociation equilibrium should gradually be shifted towards the dissociated form, keeping a smoother monomer generation rate and thus a low and more constant chemical potential over time. An additional reason to replace part of the oleic acid by sodium oleate is because it is known that the acidic form can condensate with itself at the high temperatures of the synthesis (near 300°C) *via* heterolytic cleavage (*i.e.*, ketonic decarboxylation).[42] As by-products of this reaction, a heavy ketone (oleone), CO_2 and water are generated. Reducing the occurrence of this reaction is highly desirable, since these by-products can generate abrupt bubbling, changing the local concentrations and chemical properties (adding heterogeneity to the mixture) and also because the generated water can react with dibenzyl-ether to produce benzaldehyde changing the overall polarity of the mixture or its boiling point. However, in the sodic form, the heterolytic cleavage necessary for this reaction is strongly disfavoured. Nevertheless, similarly to the case of dibenzyl ether, a total substitution of oleic acid for sodium oleate is not possible since it is poorly dissolved in the mixture at room temperature and cannot dissociate to exchange iron from iron acetylacetonate and generate the monomers. We empirically found that the number of sodium oleate moles should be around 15% of oleic acid mol. Finally, one last reason to add sodium oleate is that the sodium cations generated in the reaction are highly

hygroscopic, hence they can trap any water molecules formed during the synthesis. This avoids the reported[52] negative influence of water on the shape of the nanoparticles.

To confirm the size and shape evolution mechanism, aliquots were taken at different reflux times (after the mixture just starts to boil, at t = 0, 10, 30 and 60 min) and analysed using TEM. Although in the aliquots taken in the first 10 minutes the number of particles that could be recovered was exceedingly low (probably because due to their small size they could not be precipitated after washing) to perform any systematic analysis, the images at 30 min and 60 min confirmed the transition from octahedral into cubic structure after the first 30 minutes of reflux (Figure S11a,b). Notably, when the same experiment was carried out with only oleic acid (but keeping the total concentration of surfactant the same), the growth of the particles was faster but resulted in octahedral-shaped particles, as expected from an initially higher but much less constant μ_m during the reflux time (Figure S11c,d). In addition, in the case of oleic acid the growth was practically finished after the first 30 min and extending the reflux time to 60 min only lead to a size increase of 1 nm, whereas in the reaction with oleic acid and sodium oleate, the particles experienced more drastic size and morphology changes over time.

Discussion of the size control

There are different approaches to control the size of the nanocubes without changing the solvent or the iron precursor, like replacing oleic acid by a shorter ligand such as decanoic acid.[12] However, since decanoic acid is a shorter fatty acid than oleic acid, the steric hindrance it can provide is weaker. Taking into account the magnetic character of the final product, decanoic acid will provide less protection against aggregation due to dipolar interactions. Since our goal is having colloidally stable nanocubes, we chose oleic acid as surfactant.

The main parameter to control the size in our synthesis is the amount of iron (III) acetylacetonate. Since the limiting factor for the growth of the particles is the availability of monomers that can be incorporated into the structures, higher or lower amounts of iron precursor lead to larger or smaller nanoparticles, respectively.

Moreover, the synthetic approach has an initial stage where vacuum is done at 60°C for 1 hour to ensure the elimination of both water and oxygen traces in the solvents. During this step, the exchange between iron acetylacetonate and oleic acid is favoured, leading to the formation of monomers of iron oleate. As the temperature at which vacuum is performed increases, the number of monomers will increase. A higher number of monomers when the nucleation step begins will produce a higher number of nuclei, decreasing the amount of iron available for the later growth stage and thus leading to smaller particles. For the same reason, a slow heating rate (3°C/min) was chosen to reach the boiling temperature.

Finally, to achieve particles larger than about 25 nm a slightly modified approach is necessary. Increasing the reagent concentration (by reducing the solvent volume) allows the particles to grow for longer time because in this way a lower total number of monomers is required to have a high enough μ_m to overcome the energy barrier for the deposition on the surface of the particles. However, as mentioned before, if μ_m is too high the cubic morphology can be lost. For this reason, the heating rate was increased to (i) have a lower number of nuclei and (ii) avoid all the monomers to be generated in the same time, thus keeping a moderate μ_m for a longer time. Thus, the combination of the higher concentration and faster heating rate allows the synthesis of large nanocubes.

CONCLUSIONS

Summarizing, a synthetic approach to prepare optimal spinel oxide nanocubes with nanometrically tuneable size, while keeping a narrow distribution, has been developed. The approach allows synthesizing Fe_3O_4 nanocubes over a broad range of sizes (9 – 80 nm) with outstanding cubic morphology and a small PDI(< 10%) over the whole range of sizes. The proposed synthesis pathway is the result of a careful rational design. Thus, the use of a mixture of several solvents and the addition of Na-oleate are aimed at creating stable conditions for the stabilization of the cubic shape over a broad range of sizes. Therefore, this synthetic pathway enables the facile and accurate control of the nanocubes size, which is crucial to optimize their properties, for example, for biomedical applications. In particular, the nanocubes with an edge length below 17 nm show a great colloidal stability, even after transferring them to water, and suitable hyperthermia and NMR relaxivity performance, making them excellent candidates for potential applications in the biomedical (and other) field(s). In addition, the synthesis pathway can be easily adapted to other spinel oxides. The fine nanometric control of the nanocubes size keeping the cubic morphology over a wide range of sizes in a variety of materials makes this synthesis route very appealing for multiple applications of nanocubes.

METHODS

Materials

All chemicals, iron (III) acetylacetonate >99% (Acros Organics); cobalt (II) acetylacetonate 97% (Sigma); manganese (II) acetylacetonate (Sigma); oleic acid >90% (Sigma); dibenzyl ether >99% (Acros Organics); sodium oleate >82% (Sigma); 1-octadecene >90% (Sigma); poly(maleic anhydride-alt-1-octadecene) (Sigma); and 1-tetradecene >92% (Sigma) were used as supplied without further purification.

Note that spherical Fe_3O_4 particles were purchased from Ocean Nanotech® (see SI).

Synthesis

Fe_3O_4 nanocubes

In the standard synthesis, iron (III) acetylacetonate (0.446 g; 1.27 mmol; nominal concentration = 51.53 mM), sodium oleate (0.23g; 0.80 mmol; nominal concentration = 9.33 mM) and oleic acid (1.48 g; 5.20 mmol; nominal concentration = 210.95 mM) were added to a mixture of 1-octadecene (10 mL), dibenzyl ether (10 mL) and 1-tetradecene (3 mL).). This mixture was heated to 60 °C at a rate of 5 °C/min and kept at this temperature in vacuum (~$3 \cdot 10^{-2}$ mbar) for one hour under vigorous magnetic stirring. Subsequently, the slurry was heated up to the reflux temperature (~290 °C) at a rate of 3 °C/min under argon flow and kept at this temperature for 60 minutes. Finally, the reaction was cooled down to room temperature.

In order to purify the nanocubes, the resulting product was washed with a mixture of isopropanol (50 mL), acetone (40 mL) and methanol (10 mL) and centrifuged for 10 minutes at 10600 g, discarding the supernatant. The product was washed again with chloroform (20 mL), isopropanol (40 mL) and methanol (30 mL) and centrifuged. Finally, the nanoparticles were redispersed in toluene. This standard procedure results in iron oxide nanocubes with an average edge length of 15.3 nm.

The size could be easily tuned over a wide range by adjusting the experimental conditions: *e.g.*, amount of iron (III) acetylacetonate, heating rate, temperature at which vacuum is performed or the solvent volume. For instance, if the amount of iron (III) acetylacetonate was reduced to 0.400 g (1.12 mmol; nominal concentration = 45.44 mM) while keeping the rest of parameters unchanged, 9.1 nm nanocubes are obtained. On the other hand, 24.5 nm nanocubes were obtained when the amount of iron (III) acetylacetonate is increased up to 0.610 g (1.73 mmol; nominal concentration = 70.18 mM) and the heating rate is increased to 15 °C/min. Larger cubes (~80 nm) could be obtained by modifying the reagent concentration. Namely, iron (III) acetylacetonate (0.530 g; 1.50 mmol; nominal concentration = 120.48 mM) and oleic acid (0.85 g; 3.01 mmol; nominal concentration = 241.77 mM) are added to a mixture of 1-octadecene (5 mL), dibenzyl ether (5 mL) and 1-tetradecene (1.5 mL).. This mixture is degassed at room temperature for 60 min in vacuum. Afterwards, the blend was heated up to the reflux temperature at a rate of 20 °C/min under argon atmosphere and kept at this temperature for 60 minutes. After cooling down to room temperature, the product was centrifuged and washed with a mixture of toluene and hexane 1:1 twice. This procedure leads to cubes about 81.5 nm in edge length.

Synthesis of other spinel oxides

Cobalt ferrite and manganese ferrite nanocubes were synthesized by the same synthetic pathway used of Fe_3O_4 keeping the same number of mol of metallic precursor.

For the synthesis of cobalt ferrite nanocubes, iron (III) acetylacetonate (0.299 g, 0.85 mmol; nominal concentration = 34.48 mM) and cobalt (II) acetylacetonate (0.109 g; 0.42 mmol; nominal concentration = 17.04 mM) were mixed with sodium oleate (0.23 g, 0.8 mmol; nominal concentration = 32.45 mM), oleic acid (1.48 g, 5.2 mmol; nominal concentration = 210.95 mM) and a solvent mixture composed by 10 mL 1-octadecene, 10 mL benzyl ether and 3 mL 1-tetradecene. This mixture was heated to 60 °C at a rate of 5 °C/min and kept at this temperature in vacuum (~$3 \cdot 10^{-2}$ mbar) for one hour under vigorous magnetic stirring. Subsequently, the slurry was heated up to the reflux temperature (~290 °C) at a rate of 3 °C/min under argon flow and kept at this temperature for 60 minutes. Finally, the reaction was cooled down to room temperature. The standard procedure for cobalt ferrite leads to 13.1 nm nanocubes. The size can be tuned by changing the temperature at which the vacuum was performed. If the vacuum was performed at 40 ºC the final size increases up to 15.3 nm, whereas if the vacuum is performed at 100 ºC the final size decreases to 8.5 nm.

Manganese ferrite nanocubes were synthesized by mixing iron (III) acetylacetonate (0.299 g, 0.85 mmol; nominal concentration = 34.48 mM) and manganese (II) acetylacetonate (0.107 g; 0.42 mmol; nominal concentration = 17.04 mM) using the same amount of reactants and reaction parameters than Fe_3O_4 and cobalt ferrite. The standard synthesis of manganese ferrite leads to 11.1 nm nanocubes. When the temperature at which vacuum was performed was 100 ºC the final size downs to 6.7 nm while if it deceases to 40 ºC the final size is 13.1 nm.

In addition, nanocubes of Mn_3O_4 (a tetragonal spinel) were also synthesized using an analogous synthesis procedure. Briefly, iron (III) acetylacetonate was replaced in the standard synthesis (15.3 nm Fe_3O_4 cubes) by manganese (II) acetylacetonate (0.321 g; 1.27 mmol; nominal concentration = 51.52 mM) while keeping the rest of conditions the same.

Characterisation

Transmission Electron Microscopy (TEM)

The TEM Images were acquired using a JEOL JEM-1400 transmission microscope operating at 80 kV. The specimens for TEM imaging were prepared by dipping a carbon copper grid into a dilute suspension of the particles in toluene freshly sonicated. The average particle size and its standard deviation were estimated by measuring the edge length of at least 100 particles. Data were fitted to a log-normal function and the polydispersity index (PDI) was calculated for all the samples. High-

resolution TEM images and electron energy loss spectroscopy (EELS) mapping have been obtained using a FEI Tecnai F20 equipped with a Quantum GIF EELS spectrometer. The experiments were carried out at 200 kV. The EEL spectra were analysed using the Oxide Wizard script.[53,54]

Scanning Electron Microscopy (SEM) and energy-dispersive X-ray spectroscopy (EDX)

The specimens for SEM imaging were prepared by diluting the particles in toluene and dipping a carbon copper grid into a freshly sonicated dispersion. The images were acquired using a FEI Magellan 400L XHR scanning electron microscope equipped with an Oxford Instruments Ultim Extreme EDX detector system.

X-Ray Diffraction (XRD)

The XRD measurements were carried out using an X'pert PRO MPD from PANalytical with a Cu K_α radiation (λ = 0.15406 nm).

Magnetometry

The magnetic properties were evaluated on tightly packed powdered samples using a superconducting quantum interference device-vibrating sample magnetometer (SQUID-VSM; Quantum Design). The temperature dependence of the magnetization was recorded in H = 5 Oe while warming (10 – 350 K) after either zero field cooling (ZFC) or field cooling (FC) from 350 K to 10K in H = 5 Oe. The hysteresis loops were carried out either at room temperature or at 10 K (after field cooling in 20 kOe from 300 to 10 K) applying a maximum field of 70 kOe. The amount of organic residues (such as the surfactant), was estimated by thermogravimetric analysis (TGA) to be about 8.5%. Note that from the TGA mass loss and considering the surface area of our material, we can estimate that the adsorbed oleic acid was about 2.6 molecules/nm^2, which is consistent with literature values.[55] The contribution of organic residues was subtracted from the sample total mass for the calculation of the magnetisation of the particles.

Hydrodynamic diameter and Z-Potential measurements

The samples were dispersed either in toluene or mili-Q water prior to the measurement of the hydrodynamic diameter and the Z-Potential. The measurements were carried out in a Zetasizer Nano ZS (Malvern Panalytical).

Transfer to water

The particles were transferred to water following an amphiphilic polymer coating procedure established by Pellegrino *et al*.[56] with some modifications. Briefly, the particles were dispersed in chloroform and poly (maleic acid-alt-1-octadecene) at a ratio of 500 monomer units per nm^2 of

particles. After sonicating for 10 min, the chloroform was removed by rotaevaporation. The resulting precipitate was covered with borate buffer (50 mM at pH 9) and sonicated until the complete redispersion of the particles. The mixture was further ultrasonicated and filtrated through a syringe filter (0.22 μm pore size). Finally, the particles were centrifuged at 10600 g for 4 hours and redispersed in mili-Q water.

Magnetic hyperthermia

The heating capacity of the particles was measured by applying an alternating magnetic field, *H*, of 213 Oe (17 kA/m) at a frequency *f* = 183 kHz, using an experimental set-up based on a 6 kW Fives Celes® power supply. The sample was placed in a polystyrene sample holder inside a glass tube thermostated at 25°C using an ethylene glycol flow and the temperature was recorded through an optical fiber thermometer dipped into the sample dispersion. The total exposition to the alternating magnetic field was 5 min for each measurement. To determine the reproducibility, the measurements were collected in triplicate.

The Specific Absorption Rate (SAR) value was determined according to the relationship:

$$SAR = \frac{C_{H_2O} \cdot m_{sample}}{m_{Fe}} \frac{dT}{dt},$$

where C_{H2O} is the specific heat of water (4.18 $Jg^{-1}K^{-1}$), m_{sample} the total mass of the sample and m_{Fe} the total mass of iron in the sample. Since measurements were carried out in a non-adiabatic system, $\frac{dT}{dt}$ was extrapolated from the initial slope of the calorimetric curve.

The iron concentration in all the samples was 6.9 mg/mL, as determined by inductively coupled plasma atomic emission spectroscopy (ICP-AES).

In addition, to compare with other systems, the intrinsic loss power (ILP) was evaluated as $ILP = \frac{SAR}{H^2 f}$.[36]

Nuclear magnetic resonance (NMR)

^{1}H-Magnetic resonance imaging studies were performed in a 70 kOe Bruker BioSpec 70/30 USR For the measurement of the transversal relaxation times, T_2, phantoms containing nanoparticles at various concentrations in 1% agarose were prepared. The relaxivities, r_2, were obtained as the slope of the linear regression of the relaxation rates (R), as the inverse of the relaxation times ($R_2 = 1/T_2$) *versus* the Fe concentration.

ASSOCIATED CONTENT

Supporting information

Detailed experimental procedures and supplementary figures. This material is available free of charge *via* the Internet at http://pubs.acs.org.

EELS spectra and EELS-mapping; XRD pattern of the nanocubes; characterization of the cobalt and manganese ferrite nanocubes; discussion of the origin of the magnetically driven aggregation; characterisation of the particles after being transferred to water; characterization of the spherical particles; comparison of the relaxivities of cubes and spheres; surface-to-volume ratio plot as a function of the particle size; aliquot studies of the particle growth; summary of the different synthesis conditions.

The authors declare no competing financial interest.

AUTHOR INFORMATION

Corresponding Authors

* E-mail: javimuroc@msn.com

* E-mail: alejandrogroca@gmail.com

ORCID

Javier Muro-Cruces: 0000-0003-1857-1314

Alejandro G. Roca: 0000-0001-6610-9197

Alberto López-Ortega: 0000-0003-3440-4444

Elvira Fantechi: 0000-0002-9323-2198

D. del-Pozo-Bueno

Sonia Estradé: 0000-0002-3340-877X

Francesca Peiró: 0000-0002-5697-0554

Francesco Pineider: 0000-0003-4066-4031

Claudio Sangregorio: 0000-0002-2655-3901

Josep Nogués: 0000-0003-4616-1371

ACKNOWLEDGEMENTS

We acknowledge funding from Generalitat de Catalunya through the 2017-SGR-292 and 2017-SGR-776 projects and the Spanish Ministry of Economy, Industry and Competitiveness (MINECO) through the MAT2016-77391-R and MAT2016-79455-P projects. E.F. and F.P. acknowledge the University of Pisa for its funding through the PRA_2017_25 project. The authors thank P. Torruella and I.V. Golosovsky for useful discussions. ICN2 is funded by the CERCA Programme/Generalitat de Catalunya. ICN2 also acknowledges the support from the Severo Ochoa Program (MINECO, Grant SEV-2017-0706).

REFERENCES

(1) Burda, C.; Chen, X.; Narayanan, R.; El-Sayed, M. A. Chemistry and Properties of Nanocrystals of Different Shapes. *Chem. Rev.* **2005**, *105*, 1025–1102.

(2) Thanh, N. T. K.; Maclean, N.; Mahiddine, S. Mechanisms of Nucleation and Growth of Nanoparticles in Solution. *Chem. Rev.* **2014**, *114*, 7610–7630.

(3) Wang, J. P. FePt Magnetic Nanoparticles and Their Assembly for Future Magnetic Media. *Proc. IEEE* **2008**, *96*, 1847–1863.

(4) Lu, A.-H.; Salabas, E. L.; Schüth, F. Magnetic Nanoparticles: Synthesis, Protection, Functionalization, and Application. *Angew. Chemie Int. Ed.* **2007**, *46*, 1222–1244.

(5) Khin, M. M.; Nair, A. S.; Babu, V. J.; Murugan, R.; Ramakrishna, S. A Review on Nanomaterials for Environmental Remediation. *Energy Environ. Sci.* **2012**, *5*, 8075–8109.

(6) Rocha-Santos, T. A. P. Sensors and Biosensors Based on Magnetic Nanoparticles. *TrAC - Trends Anal. Chem.* **2014**, *62*, 28–36.

(7) Reddy, L. H.; Arias, J. L.; Nicolas, J.; Couvreur, P. Magnetic Nanoparticles: Design and Characterization, Toxicity and Biocompatibility, Pharmaceutical and Biomedical Applications. *Chem. Rev.* **2012**, *112*, 5818–5878.

(8) Laurent, S.; Forge, D.; Port, M.; Roch, A.; Robic, C.; Vander Elst, L.; Muller, R. N. Magnetic Iron Oxide Nanoparticles: Synthesis, Stabilization, Vectorization, Physicochemical Characterizations, and Biological Applications. *Chem. Rev.* **2010**, *110*, 2574–2574.

(9) Ling, D.; Hyeon, T. Chemical Design of Biocompatible Iron Oxide Nanoparticles for Medical Applications. *Small* **2013**, *9*, 1450–1466.

(10) Bobo, D.; Robinson, K. J.; Islam, J.; Thurecht, K. J.; Corrie, S. R. Nanoparticle-Based Medicines: A Review of FDA-Approved Materials and Clinical Trials to Date. *Pharm. Res.* **2016**, *33*, 2373–2387.

(11) Geng, Y. A. N.; Dalhaimer, P.; Cai, S.; Tsai, R.; Minko, T.; Discher, D. E. Shape Effects of Filaments *versus* Spherical Particles in Flow and Drug Delivery. *Nat. Nanotechnol.* **2007**, *2*, 249–255.

(12) Guardia, P.; Di Corato, R.; Lartigue, L.; Wilhelm, C.; Espinosa, A.; Garcia-Hernandez, M.; Gazeau, F.; Manna, L.; Pellegrino, T. Water-Soluble Iron Oxide Nanocubes with High Values of Specific Absorption Rate for Cancer Cell Hyperthermia Treatment. *ACS Nano* **2012**, *6*, 3080–3091.

(13) Nemati, Z.; Alonso, J.; Rodrigo, I.; Das, R.; Garaio, E.; García, J. Á.; Orue, I.; Phan, M.-H.; Srikanth, H. Improving the Heating Efficiency of Iron Oxide Nanoparticles by Tuning Their Shape and Size. *J. Phys. Chem. C* **2018**, *122*, 2367–2381.

(14) Cho, M.; Cervadoro, A.; Ramirez, M.; Stigliano, C.; Brazdeikis, A.; Colvin, V.; Civera, P.; Key, J.; Decuzzi, P. Assembly of Iron Oxide Nanocubes for Enhanced Cancer Hyperthermia and Magnetic Resonance Imaging. *Nanomaterials* **2017**, *7*, 72.

(15) Lisjak, D.; Mertelj, A. Anisotropic Magnetic Nanoparticles: A Review of Their Properties, Syntheses and Potential Applications. *Prog. Mater. Sci.* **2018**, *95*, 286–328.

(16) Salazar-Alvarez, G.; Qin, J.; Šepelák, V.; Bergmann, I.; Vasilakaki, M.; Trohidou, K. N.; Ardisson, J. D.; Macedo, W. A. A.; Mikhaylova, M.; Muhammed, M.; Baró, M. D.; Nogués, J. Cubic *versus* Spherical Magnetic Nanoparticles: The Role of Surface Anisotropy. *J. Am. Chem. Soc.* **2008**, *130*, 13234–13239.

(17) Mitra, A.; Mohapatra, J.; Meena, S. S.; Tomy, C. V.; Aslam, M. Verwey Transition in Ultrasmall-Sized Octahedral Fe_3O_4 Nanoparticles. *J. Phys. Chem. C* **2014**, *118*, 19356–19362.

(18) Mirabello, G.; Lenders, J. J. M.; Sommerdijk, N. A. J. M. Bioinspired Synthesis of Magnetite Nanoparticles. *Chem. Soc. Rev.* **2016**, *45*, 5085–5106.

(19) Andrés Vergés, M.; Costo, R.; Roca, A. G.; Marco, J. F.; Goya, G. F.; Serna, C. J.; Morales, M. P. Uniform and Water Stable Magnetite Nanoparticles with Diameters around the Monodomain–Multidomain Limit. *J. Phys. D. Appl. Phys.* **2008**, *41*, 134003.

(20) Kim, D.; Lee, N.; Park, M.; Kim, B. H.; An, K.; Hyeon, T. Synthesis of Uniform Ferrimagnetic Magnetite Nanocubes. *J. Am. Chem. Soc.* **2009**, *131*, 454–455.

(21) Kovalenko, M. V.; Bodnarchuk, M. I.; Lechner, R. T.; Hesser, G.; Schäffler, F.; Heiss, W. Fatty Acid Salts as Stabilizers in Size- and Shape-Controlled Nanocrystal Synthesis: The Case of Inverse Spinel Iron Oxide. *J. Am. Chem. Soc.* **2007**, *129*, 6352–6353.

(22) Estrader, M.; López-Ortega, A.; Golosovsky, I. V.; Estradé, S.; Roca, A. G.; Salazar-Alvarez, G.; López-Conesa, L.; Tobia, D.; Winkler, E.; Ardisson, J. D.; Macedo, W. a. a.; Morphis, A.; Vasilakaki, M.; Trohidou, K. N.; Gukasov, A.; Mirebeau, I.; Makarova, O. L.; Zysler, R. D.; Peiró, F. *et al*. Origin of the Large Dispersion of Magnetic Properties in Nanostructured Oxides: Fe_xO/Fe_3O_4 Nanoparticles as a Case Study. *Nanoscale* **2015**, *7*, 3002–3015.

(23) Torruella, P.; Arenal, R.; de la Peña, F.; Saghi, Z.; Yedra, L.; Eljarrat, A.; López-Conesa, L.; Estrader, M.; López-Ortega, A.; Salazar-Alvarez, G.; Nogués, J.; Ducati, C.; Midgley, P. a.; Peiró, F.; Estradé, S. 3D Visualization of the Iron Oxidation State in FeO/Fe_3O_4 Core–Shell Nanocubes from Electron Energy Loss Tomography. *Nano Lett.* **2016**, *16*, 5068–5073.

(24) Ichikawa, R. U.; Roca, A. G.; López-Ortega, A.; Estrader, M.; Peral, I.; Turrillas, X.; Nogués, J. Combining X-Ray Whole Powder Pattern Modeling, Rietveld and Pair Distribution Function Analyses as a Novel Bulk Approach to Study Interfaces in Heteronanostructures: Oxidation Front in FeO/Fe_3O_4 Core/Shell Nanoparticles as a Case Study. *Small* **2018**, *14*, 1800804.

(25) Feld, A.; Weimer, A.; Kornowski, A.; Winckelmans, N.; Merkl, J.-P.; Kloust, H.; Zierold, R.; Schmidtke, C.; Schotten, T.; Riedner, M.; Bals, S.; Weller, H. Chemistry of Shape-Controlled Iron Oxide Nanocrystal Formation. *ACS Nano* **2019**, *13*, 152–162.

(26) Wetterskog, E.; Tai, C.-W.; Grins, J.; Bergström, L.; Salazar-Alvarez, G. Anomalous Magnetic Properties of Nanoparticles Arising from Defect Structures: Topotaxial Oxidation of $Fe_{1-x}O|Fe_{3-\delta}O_4$ Core|Shell Nanocubes to Single-Phase Particles. *ACS Nano* **2013**, *7*, 7132–7144.

(27) Guardia, P.; Riedinger, A.; Nitti, S.; Pugliese, G.; Marras, S.; Genovese, A.; Materia, M. E.; Lefevre, C.; Manna, L.; Pellegrino, T. One Pot Synthesis of Monodisperse Water Soluble Iron Oxide Nanocrystals with High Values of the Specific Absorption Rate. *J. Mater. Chem. B* **2014**, *2*, 4426–4434.

(28) Qiao, L.; Fu, Z.; Li, J.; Ghosen, J.; Zeng, M.; Stebbins, J.; Prasad, P. N.; Swihart, M. T. Standardizing Size- and Shape-Controlled Synthesis of Monodisperse Magnetite (Fe_3O_4) Nanocrystals by Identifying and Exploiting Effects of Organic Impurities. *ACS Nano* **2017**, *11*, 6370–6381.

(29) Disch, S.; Wetterskog, E.; Hermann, R. P.; Salazar-Alvarez, G.; Busch, P.; Brückel, T.; Bergström, L.; Kamali, S. Shape Induced Symmetry in Self-Assembled Mesocrystals of Iron Oxide Nanocubes. *Nano Lett.* **2011**, *11*, 1651–1656.

(30) Frison, R.; Cernuto, G.; Cervellino, A.; Zaharko, O.; Colonna, G. M.; Guagliardi, A.; Masciocchi, N. Magnetite–Maghemite Nanoparticles in the 5–15 nm Range: Correlating the Core–Shell Composition and the Surface Structure to the Magnetic Properties. A Total Scattering Study. *Chem. Mater.* **2013**, *25*, 4820–4827.

(31) Walz, F. The Verwey Transition - a Topical Review. *J. Phys. Condens. Matter* **2002**, *14*, R285–R340.

(32) Liu, X. L.; Fan, H. M. Innovative Magnetic Nanoparticle Platform for Magnetic Resonance Imaging and Magnetic Fluid Hyperthermia Applications. *Curr. Opin. Chem. Eng.* **2014**, *4*, 38–46.

(33) Almeida, T. P.; Muxworthy, A. R.; Kovács, A.; Williams, W.; Brown, P. D.; Dunin-Borkowski, R. E. Direct Visualization of the Thermomagnetic Behavior of Pseudo–Single-Domain Magnetite Particles. *Sci. Adv.* **2016**, *2*, e1501801.

(34) Hergt, R.; Dutz, S. Magnetic Particle Hyperthermia-Biophysical Limitations of a Visionary Tumour Therapy. *J. Magn. Magn. Mater.* **2007**, *311*, 187–192.

(35) Lacroix, L.-M.; Malaki, R. B.; Carrey, J.; Lachaize, S.; Respaud, M.; Goya, G. F.; Chaudret, B. Magnetic Hyperthermia in Single-Domain Monodisperse FeCo Nanoparticles: Evidences for Stoner–Wohlfarth Behavior and Large Losses. *J. Appl. Phys.* **2009**, *105*, 023911.

(36) Kallumadil, M.; Tada, M.; Nakagawa, T.; Abe, M.; Southern, P.; Pankhurst, Q. a. Suitability of Commercial Colloids for Magnetic Hyperthermia. *J. Magn. Magn. Mater.* **2009**, *321*, 1509–1513.

(37) Marcelo, G.; Catalina, F.; Bruvera, I.; Marquina, C.; Goya, G. Specific Power Absorption of Silica-Coated Magnetite Cubes. *Curr. Nanosci.* **2014**, *10*, 676–683.

(38) Espinosa, A.; Di Corato, R.; Kolosnjaj-Tabi, J.; Flaud, P.; Pellegrino, T.; Wilhelm, C. Duality of Iron Oxide Nanoparticles in Cancer Therapy: Amplification of Heating Efficiency by Magnetic Hyperthermia and Photothermal Bimodal Treatment. *ACS Nano* **2016**, *10*, 2436–2446.

(39) Keisari, Y. *Tumor Ablation*; Keisari, Y., Ed.; Springer Netherlands: Dordrecht, 2013.

(40) Guibert, C.; Dupuis, V.; Peyre, V.; Fresnais, J. Hyperthermia of Magnetic Nanoparticles: Experimental Study of the Role of Aggregation. *J. Phys. Chem. C* **2015**, *119*, 28148–28154.

(41) Lee, N.; Choi, Y.; Lee, Y.; Park, M.; Moon, W. K.; Choi, S. H.; Hyeon, T. Water-Dispersible Ferrimagnetic Iron Oxide Nanocubes with Extremely High r_2 Relaxivity for Highly Sensitive *In Vivo* MRI of Tumors. *Nano Lett.* **2012**, *12*, 3127–3131.

(42) Kemp, S. J.; Ferguson, R. M.; Khandhar, A. P.; Krishnan, K. M. Monodisperse Magnetite Nanoparticles with Nearly Ideal Saturation Magnetization. *RSC Adv.* **2016**, *6*, 77452–77464.

(43) Hyeon, T.; Su Seong Lee; Park, J.; Chung, Y.; Hyon Bin Na. Synthesis of Highly Crystalline and Monodisperse Maghemite Nanocrystallites without a Size-Selection Process. *J. Am. Chem. Soc.* **2001**, *123*, 12798–12801.

(44) Levy, M.; Quarta, A.; Espinosa, A.; Figuerola, A.; Wilhelm, C.; García-Hernández, M.; Genovese, A.; Falqui, A.; Alloyeau, D.; Buonsanti, R.; Cozzoli, P. D.; García, M. A.; Gazeau, F.; Pellegrino, T. Correlating Magneto-Structural Properties to Hyperthermia Performance of Highly Monodisperse Iron Oxide Nanoparticles Prepared by a Seeded-Growth Route. *Chem. Mater.* **2011**, *23*, 4170–4180.

(45) Gilbert, K. E.; Gajewski, J. J. Coal Liquefaction Model Studies: Free Radical Chain Decomposition of Diphenylpropane, Dibenzyl Ether, and Phenyl Ether *via β*-Scission Reactions. *J. Org. Chem.* **1982**, *47*, 4899–4902.

(46) Moya, C.; Batlle, X.; Labarta, A. The Effect of Oleic Acid on the Synthesis of Fe_{3-x} O_4 Nanoparticles over a Wide Size Range. *Phys. Chem. Chem. Phys.* **2015**, *17*, 27373–27379.

(47) Barbieri, a.; Weiss, W.; Van Hove, M. a.; Somorjai, G. a. Magnetite Fe_3O_4(111): Surface Structure by LEED Crystallography and Energetics. *Surf. Sci.* **1994**, *302*, 259–279.

(48) LaMer, V. K.; Dinegar, R. H. Theory, Production and Mechanism of Formation of Monodispersed Hydrosols. *J. Am. Chem. Soc.* **1950**, *72*, 4847–4854.

(49) Lee, J.; Yang, J.; Kwon, S. G.; Hyeon, T. Nonclassical Nucleation and Growth of Inorganic Nanoparticles. *Nat. Rev. Mater.* **2016**, *1*, 16034.

(50) Peng, Z. A.; Peng, X. Mechanisms of the Shape Evolution of CdSe Nanocrystals. *J. Am. Chem. Soc.* **2001**, *123*, 1389–1395.

(51) Wang, Y.; He, J.; Liu, C.; Chong, W. H.; Chen, H. Thermodynamics *versus* Kinetics in Nanosynthesis. *Angew. Chemie - Int. Ed.* **2015**, *54*, 2022–2051.

(52) Cotin, G.; Kiefer, C.; Perton, F.; Ihiawakrim, D.; Blanco-Andujar, C.; Moldovan, S.; Lefevre, C.; Ersen, O.; Pichon, B.; Mertz, D.; Bégin-Colin, S. Unravelling the Thermal Decomposition Parameters for The Synthesis of Anisotropic Iron Oxide Nanoparticles. *Nanomaterials* **2018**, *8*, 881.

(53) Yedra, L.; Xuriguera, E.; Estrader, M.; López-Ortega, A.; Baró, M. D.; Nogués, J.; Roldan, M.; Varela, M.; Estradé, S.; Peiró, F. Oxide Wizard: An EELS Application to Characterize the White Lines of Transition Metal Edges. *Microsc. Microanal.* **2014**, *20*, 698–705.

(54) Colliex, C.; Manoubi, T.; Ortiz, C. Electron-Energy-Loss-Spectroscopy Near-Edge Fine Structures in the Iron-Oxygen System. *Phys. Rev. B* **1991**, *44*, 11402–11411.

(55) Klokkenburg, M.; Hilhorst, J.; Erné, B. H. Surface Analysis of Magnetite Nanoparticles in Cyclohexane Solutions of Oleic Acid and Oleylamine. *Vib. Spectrosc.* **2007**, *43*, 243–248.

(56) Pellegrino, T.; Manna, L.; Kudera, S.; Liedl, T.; Koktysh, D.; Rogach, A. L.; Keller, S.; Rädler, J.; Natile, G.; Parak, W. J. Hydrophobic Nanocrystals Coated with an Amphiphilic Polymer Shell: A General Route to Water Soluble Nanocrystals. *Nano Lett.* **2004**, *4*, 703–707.

For Table of Contents Only